Imaging water ingress into concrete using electrical resistance tomography

B. Suryanto*, D. Saraireh, J. Kim, W.J. McCarter, G. Starrs, H. M. Taha

Heriot-Watt University,

School of Energy, Geoscience, Infrastructure and Society,

Edinburgh, EH14 4AS,

U.K.

* Corresponding Author

E-mail: b.suryanto@hw.ac.uk

Tel: +44 (0)131 451 3817

Fax: +44 (0)131 451 4617

Abstract

This paper investigates the feasibility of imaging the movement of water into partially saturated concrete using electrical resistance tomography (ERT). With this technique, the spatial distribution of electrical resistance within the concrete sample was acquired from 4-point electrical measurements obtained on its surface. As the ingress of water influences the electrical properties of the concrete, it is shown that ERT can assist in monitoring and visualising water movement within concrete. To this end, the *difference-imaging* technique was used to obtain a qualitative representation of moisture distribution within concrete during the initial 20-hour absorption. It is shown that the technique also enables the influence of surface damage to be studied.

Keywords Electrical methods, tomography, imaging, water ingress.

1 Introduction

Concrete in the near surface region plays a key role in the long-term durability of reinforced concrete structures [1, 2]. It provides the only protective barrier to the steel reinforcement from the ingress of water, and water containing deleterious ionic species such as chlorides, which may, eventually, initiate corrosion [3–5]. The quality of concrete cover depends largely on the porous nature of the concrete in this region which is determined largely by the interconnectivity of the capillary pore network within the cementitious binder. Furthermore, during the lifetime of a structure, surface damage may occur due to numerous factors, including restrained shrinkage [6, 7], freeze-thaw [8, 9], alkali-silica reaction [10] and in-service loading [11, 12], which all may negate the role of the concrete cover as the protective barrier to the steel. In this context, being able to monitor, quantify and visualise the response of concrete in the cover region to the external environment could be of considerable benefit in the development and design of durable concretes.

A variety of investigative techniques have now been developed to study the permeation properties of concrete in the surface region, with some being no longer confined to laboratory studies and used in real structures. The performance of these investigative techniques are well-documented and can be found in various state-of-the-art reports (see, for example, [13]). Given the importance of cover-zone concrete, this topic still remains the subject of research and development and new techniques are currently being developed to provide an improvement over existing technologies. One such emerging technology is electrical impedance tomography (EIT) which has been extensively used in medical, geophysical and industrial process fields. Karhunen et al [14] were amongst the first to employ this investigative technique to detect conductive/non-conductive objects embedded inside cylindrical concrete specimens. It was noted that electrical resistance tomography (ERT) could be further developed as a means of assessing the extent of corrosion of embedded reinforcement in concrete; for this specific application, Zhang et al [15] proposed the use of high-frequency electrical measurements to alleviate the likelihood presence of micro-cracking surrounding the reinforcement. The use of ERT has also been investigated as a means of tracking one- and two-dimensional moisture movement within cement-paste prisms [16], with the reconstructed images shown to be in a good agreement with those obtained from neutron radiographic measurements. Building upon this work, Smyl et al [17] used a three-dimensional ERT system to obtain the movement of moisture in cylindrical mortars with both artificial and real discrete cracks. Apart from studying moisture movement in cement-based materials, ERT has also been used for crack detection [see, for example, 18–20] and obtaining the distribution of resistivity within the cover-zone [21].

The work in this paper builds upon previous studies on monitoring the response of the concrete cover-zone to a cyclic wetting and drying regime [22–24]. An ERT system is developed to allow imaging of water ingress into concrete and preliminary findings are presented to show the temporal response of a concrete cylinder containing surface damage to wetting action.

2 Electrical Resistance Tomography (ERT)

ERT is a non-invasive imaging technique whereby the distribution of the electrical conductivity within an object is estimated from surface measurements along the boundary of the object. This image reconstruction process is referred to as the inverse analysis and requires a forward model. A brief review is provided below.

2.1 Forward model

The governing partial differential equation to describe the relation between the electrical field in a 3D domain, Ω, and the resulting potential, u, on the boundary is given in [25], which can be written,

$$\nabla \cdot \sigma(x)\, \nabla \mathrm{u}(x) = 0, \quad x \in \Omega \tag{1}$$

This equation has an infinite number of solutions and requires boundary information. If S is the surface where electrodes is located, the current flux flowing to/from the l_{th} electrode is [26]

$$I_l = \int_{E_l} \sigma \frac{\partial u(x)}{\partial \bar{n}}\, dS, \quad S \in \cup_{l=1}^{L} E_L \tag{2}$$

and the current density between the electrodes is zero [26], viz,

$$\sigma \frac{\partial u(x)}{\partial \bar{n}} = 0, \qquad \partial\Omega \backslash \cup_{l=1}^{L} E_L \tag{3}$$

In these equations, $\partial\Omega$ is domain boundary, σ is the electrical conductivity, u is the electrical potential, $\bar{n}$ is the outward unit normal vector, and E_l is l_{th} electrode. The value of potential on the l_{th} electrode, V_l,, is equal to the sum of the potential on the boundary area which is in contact with the electrode, u, and the potential drop resulting from the contact impedance, z_l [26],

$$V_l = u(x) + z_l \sigma \frac{\partial u(x)}{\partial \bar{n}}, \quad x \in E_L \ , l = 1, \dots, L \tag{4}$$

It has been shown that these equations have a unique solution when the current conservation law is fulfilled,

$$\sum_{l=1}^{L} I_l = 0 \tag{5}$$

and the ground is equal to the sum of boundary potentials,

$$\sum_{l=1}^{L} V_l = 0 \tag{6}$$

By discretizing the 3D domain into small elements, Equations (1) to (6) can be solved numerically in the form of a linear equation, as given by [25]

$$\begin{bmatrix} A_c & A_e \\ A_e^T & A_d \end{bmatrix} \begin{bmatrix} u_n \\ V_l \end{bmatrix} = \begin{bmatrix} 0 \\ I_l \end{bmatrix} \quad (7)$$

where A is the global admittance matrix, u_n is the nodal potential distribution, V_l and I_l are, respectively, the boundary electrode potentials and currents. The local admittance matrix is then given by,

$$A_c(i,j) = \int_\Omega \sigma \nabla\phi_i \cdot \nabla\phi_j d\Omega + \sum_{l=1}^{L} \frac{1}{z_l} \int_{El} \phi_i \phi_j dS \quad (8)$$

where ϕ_i and ϕ_j are the element shape functions and $i, j = 1, \ldots, n$. The first term considers the electrical field in each element, while the second term considers the contribution of contact impedance underneath the electrodes which forms the other two compartments of the A matrix [25],

$$A_e(i,j) = \frac{1}{(z_l)_j} \int_{El} \phi_i \, dS \quad (9)$$

$$A_d(i,l) = \begin{cases} |E_l| z_l^{-1} & for\ i = l \\ 0 & otherwise \end{cases} \quad (10)$$

where $|E_l|$ denotes the surface area of l_{th} electrode.

2.2 Inverse analysis

The purpose of an inverse analysis, or image reconstruction, is to obtain the conductivity distribution, σ, within the medium from surface potential measurements, V. It is a highly ill-posed problem, implying that, from a given set of data, there are many possible solutions and they are sensitive to measurement noise. The most commonly used image reconstruction algorithms are *difference-imaging* and *absolute-imaging* [27]. In the *difference-imaging* method, the temporal change in response is reconstructed based on the difference between two sets of data, with the first serving as the reference. This imaging technique is more tolerant to measurement noise and experiment errors such as and variations in electrode dimension and position. However, this technique can only provide qualitative reconstruction. *Absolute-imaging*, on the other hand, can provide a quantitative reconstruction, but is more expensive computationally and more sensitive to experiment errors. While *absolute-imaging* requires only one set of measurement data, it also needs an estimate of the value of contact impedance and the precise position of the electrodes.

Numerous inverse analysis algorithms have been developed and one of the most commonly used algorithms is the one-step linear Gauss-Newton method [27]. In this approach, the relation between boundary measurements, V_m, and internal conductivity, σ, is given by

$$V_m = J\sigma + n \quad (11)$$

where J is the Jacobian matrix and n is the measurement noise (uncorrelated white Gaussian) [27]. The Jacobian matrix can be computed numerically based on the type and number of elements in the finite element model, current injection patterns and electrode models. Adler and Guardo [27] demonstrated that by employing the regularized linear inverse analysis, it is possible to relate the potential measurements V_m to a reconstructed image, $\hat{\sigma}$, and solve them in one-step analysis

$$\hat{\sigma} = (J^T W J + \lambda^2 R)^{-1} J^T W V_m \quad (12)$$

where $W = (\sigma_n^2 \sum_n)^{-1}$, $R = (\sigma_x^2 \sum_x)^{-1}$, and λ is the regularized hyperparameter ($= {}^{\sigma_n}/_{\sigma_x}$), with σ_n representing the average amplitude of measurement noise and σ_x representing the *a priori* amplitude of conductivity change.

3 Experimental Programme

3.1 Measurement system

The measurement system used in the current work comprises four main components: an Agilent 4263B LCR meter; an HP 34970A multiplexing switch control unit incorporating three 34901A modules; a desktop computer (PC) and a sample test cell containing a 16-electrode array (see Figs. 1 and 2). Communication with the measurement and multiplexing instruments was established across a GPIB system, which was accessed by the PC via an Agilent 82357A USB/GPIB interface using Keysight IO Library Suite software.

In order to manage the overall running of the measurement system, a fully automated data acquisition and control system was developed using LabView. This system facilitates the injection of current and subsequent potential measurements at repeated time interval, allowing virtually continuous monitoring of processes/variations in the material under test. In the present study, both injection and measurement protocols were set following the adjacent pattern [28], which was chosen for its simplicity. One measurement cycle typically involved 16 current injections and 13 potential readings for each current injection, thereby resulting in a total of 208 readings. Each measurement cycle took approximately 35 seconds to complete. To facilitate ERT measurements, the 4263B LCR meter was used in 4-point mode, with the current generated at the input terminals by a constant voltage of 350mV rms operating at a frequency of 1kHz, and with the potential monitored separately at the sense terminals. It provided an output value of resistance computed automatically from the injected current and measured potential.

174 The test cell was a 5mm thick cylindrical PVC mould, with an internal diameter of 154mm and a height of
175 150mm (see Fig. 3(a)). The mould was glued to a square 5mm thick PVC base-plate of edge length of 180mm.
176 At the mid height of the mould, 16 equally spaced 2mm-diameter stainless steel pins (Grade 316) were inserted
177 through the vertical wall of the mould to an inner penetration depth of 5mm, with each pin protruded 8mm from
178 the external surface to facilitate alligator clip connection. This cell, hereafter referred to as the water cell, was
179 used to perform two trial tests described in more detail in Section 3.4. The same cell was then used to monitor
180 moisture ingress in concrete, but with a 60mm diameter PVC pipe added to the centre of the base-plate, in order
181 to form a centre hole into the sample (discussed below), referred hereafter to as the concrete cell.

182

183 **3.2 Materials and sample preparation**

184 The mix proportions used in the experimental program are presented in Table 1. The mix had a water/cement
185 (w/c) ratio of 0.7 and used CEM I 52.5N cement clinker to EN197-1 [29] as the binder. The oxide composition
186 of the cement is presented in Table 2. A graded crushed granite coarse aggregate (≤10mm), fine aggregate
187 (<4mm) and tap water were used. The coarse and fine aggregates were thoroughly washed prior to use to
188 remove any silt and clay, and conditioned to a saturated, surface-dry state. A hollow cylinder (i.e. the PVC pipe
189 noted above) was cast into the mould shown in Fig. 3(b), together with three 100mm cubes for compressive
190 strength tests.

191 During fabrication, fine aggregate, cement, and water were initially mixed in a 10-litre Hobart planetary
192 mixer for 2 min. The coarse aggregate was then added into the mixing bowl and mixed manually for a further 5
193 min. The fresh concrete was then cast into the PVC mould and compacted on a vibrating table. Immediately
194 after compacting, the top surface of the specimen was covered with plastic sheeting to prevent evaporation. The
195 plastic sheeting was removed after 24h and the specimen was then submerged in water in a controlled laboratory
196 environment (20±2^{o}C) for a further 27 days; after this time, the inner PVC pipe was removed and the top and
197 bottom surfaces were then sealed with two coats of an epoxy-based paint to facilitate one dimensional drying
198 and wetting. The specimen was then left in the laboratory (55±5% RH) for 3 months, in order to allow the
199 specimen to dry naturally from the centre hole. It was noticed that part of the internal wall of the centre hole
200 sustained a certain degree of surface damage during the PVC-tube removal process, as indicated by the rather
201 rough and uneven surface (see Fig. 3(c)) observed primarily between electrode positions 2 and 5 (see Fig. 1).

In order to obtain an indication of the extent of the damage, Fig. 4 presents the resistivity of the concrete, ρ (Ωm), for each electrode pair after the specimen being left in the laboratory environment for 3 months. The resistivity was obtained from the measured electrical resistance of the concrete, R (Ω), and a calibration factor which was first determined by electrical measurements on solutions of known resistivity placed within the test-cell shown in Fig. 3(a) prior to casting. As surface defects could be expected to alter the drying processes, this would have the effect of changing the level of pore saturation and thereby altering the resistivity of the concrete in this region. Considering Fig. 4, it is evident that the average resistivity values between electrodes 1 and 6 are approximately 25% higher than those of the remaining part of the specimen, indicating that the concrete in that region is in a drier state than the remaining part of the specimen.

3.3 Wetting protocol and testing regime

The wetting process was started by filling the centre hole of the specimen by tap water (≈170 Ωm). The water had been stored in a sealed plastic container and placed next to the specimen to ensure that the influence of temperature during testing was minimal. Electrical measurements were undertaken every 40-sec interval during the initial one hour after wetting; afterwards, measurements were taken continuously on a 5-min cycle until 20-hrs.

3.4 Data processing and image reconstruction

The image reconstruction was carried out using the open-source EIT image reconstruction software EIDORS Version 3.8 [30, 31]. Initially, in order to verify and demonstrate the applicability of the measurement system and data processing procedures, two series of trial tests were firstly carried out using the test cell shown in Fig. 3(a), with tap water (≈170 Ωm) being used as the background medium. The first series of tests investigated the basic feature of the system in detecting an object placed in the medium at varied positions; for this purpose, a 48mm PVC pipe was placed in two different locations (in front of electrodes 1 and 9). The second series of tests was carried out using PVC pipes of different diameters (48mm, 64mm and 88mm) placed centrally in the test cell, which was carried out to simulate the radial, outward movement of water in the main experiment and discussed below.

To perform an ERT analysis, the basic 2D circular model template – the ‘mk_common_model’ – was used, employing 1,600 first-order triangular elements and complete electrode model (2 nodes per electrodes); no

attempt was made to model the actual geometry of the pins used in the current study. An inverse analysis was then performed using the basic 'inv_solve' function, with the option being set to the *difference-imaging*. Default parameters were used, including the 1st order for the forward calculation and matrix computation, the basic GN one-step difference solver with Laplace prior [27] and a default hyperparameter value of 0.03. The measured values obtained from the water (without any object) was used as the reference data for subsequent image reconstruction.

In the present study, the resistance values obtained from the measurements described in Section 3.1 were fed directly into the software in the place of raw potential measurement data. This is to accommodate the fact that the injected current is produced by a fixed voltage source and therefore will vary with differing material conductivity properties. In this instance, the computed resistance values can be considered as a scaled replica of the potential values which would be obtained from by a system employing a constant current source.

For the analysis of the main experiment (the hollow cylindrical specimen), it was considered appropriate to treat the specimen as a two-dimensional object, provided that there was only one layer of electrodes in the test cell. The same analysis parameters to those employed in the trial analysis were used, with the data obtained just prior to wetting being used as the reference data for image reconstruction analysis. In the present study, no attempts were made to explicitly model the core and to extract the influence of the initial moisture gradient resulting from the 3-month period of drying.

4 Results and discussion

4.1 Water cell

Figure 5(a) compares the reconstructed images and the actual position of the 48-mm diameter PVC pipe which was placed in front of electrode 1 and 9, respectively. It is evident that the actual position of the PVC pipe, which is indicated by a dashed line, is represented by a region of high resistivity (dark red and red), surrounded by a less-resistive region (yellow) and a weak development of slightly conductive zone (cyan) – an artefact feature called ringing/overshoot [32]. Another weak development of smeared artefact could also be seen near the boundary, as indicated by the region of a less-resistive region (yellow) in front of either electrodes 16, 1 and 2 or electrodes 8, 9 and 10. Despite the development of these artefacts in the background, a reasonable accuracy is indicated.

Figure 5(b) presents the results of further verification for detecting a PVC pipe of different diameters placed centrally within the test cell, with the actual size of the pipe indicated with a dashed circle. Considering that the

boundary of the region of high resistivity (red) representing the actual size of the pipe (as shown previously in Fig. 5(a)), it is evident from this Figure that the adopted technique, whilst the sensitivity at the centre can be expected at the lowest [33, 34], is still capable of detecting the change in pipe diameter. Again, reasonable accuracy is indicated, although the technique tends to overestimate the size of the smallest pipe (48mm) and underestimate the size of the largest pipe (88mm). It is also evident that the resistance along the boundary region decreases, particularly when the 88mm PVC pipe is used. This is again a 'ringing' reconstruction artefact and represents the limitation of the current system, provided that the same water was used as the background medium.

4.2 Concrete cell

4.2.1 General electrical response

The electrical response of the concrete is firstly presented to assist interpretation the results obtained from the tomography measurements. The change in *normalised* resistivity over the initial 20-hr period of absorption is presented in Fig. 6, with only data from two adjacent pairs of electrodes being plotted for illustrative purposes. The normalised resistance is defined as the ratio R_t/R_o, where R_t is the resistance at time, t, and R_0 is the resistance just before the water being poured into the centre hole. For clarity, the values obtained from the right-half side of the specimen are presented in Fig. 6(a), whereas those obtained from the left-half side are presented in Fig. 6(b).

It is evident from these Figures that as water is absorbed into the concrete, normalised resistivity values display a general decrease with time, with the concrete close to the inner surface defect (between electrodes 2 and 6) undergoing more significant reductions. Consider, for example, readings obtained from electrodes 4-5 in which N_t remains constant until about 1 hour; at 4-hrs, N_t has reduced to 0.9; 0.75 at 8-hrs; 0.62 at 12-hrs; ~0.55 at 16-hrs; and ~0.5 at 20-hrs. Electrodes 8-9, on the other hand, display a detectable increase in resistance before decreasing to the initial value before wetting at about 3.5-hrs; at 8-hrs, N_t has decreased to 0.9; 0.8 at 12-hrs; ~0.7 at 16-hrs and ~0.68 at 20-hrs. Similarly, electrodes 9-10 display a slight increase in resistance (up to 3%) before decreasing to the initial value before wetting at ~5.5-hrs; at 8-hrs, however, N_t has only decreased to 0.95; 0.87 at 12-hrs; ~0.8 at 16-hrs; and 0.72 at 20-hrs. The increase in resistance noted above could be due to the fact that as the water moves into the partially saturated concrete, it *pushes* air into the pore system thereby causing a transitory increase in resistance [35, 36].

4.2.2 Tomography results

Figure 7 displays the spatial distribution of electrical resistance within the hollow concrete cylinder over the 20-hrs after gauging, with all images reconstructed based upon the reference image which was processed from the measurements just prior to wetting. For illustrative purpose, the actual diameter of the hole (60mm) is indicated by a dotted circle, with two other dashed circles added to indicate a depth of 10mm and 20mm from the exposed (internal) working surface. It is evident from this Figure that the water in the central cavity is represented with a region of low resistivity (blue).

As the water permeates through the concrete, a traceable decrease in resistivity should follow the water front and the reconstructed images over time would, therefore, depict a blue area of low resistivity gradually expanding outwards. Examination of the images presented in Figure 7 reveals that although not that obvious, there is a general progressive enlargement of the blue region with time, particularly over the initial 4-hrs absorption. The enlargement in diameter implies that the bulk resistivity of the concrete within the surface zone (i.e., ~20mm from the exposed surface) must be higher than the resistivity of the tap water (≈170 Ωm). Given that the bulk resistivity of the concrete measured from the outer circumferential surface is within the range 53–88 Ωm (see Fig. 4), which is lower than the tap water, this would indicate the presence of a moisture gradient through the concrete. This occurred as the PVC mould was left in place over the entire period of drying prior to the absorption test. This feature is well-documented and has been observed in the cover-zone of concrete when subjected to drying [22, 23, 35, 36]. The slight enlargement in diameter over the initial 4-hrs is not entirely unexpected as the ingress is primarily driven by the moisture gradient.

The influence of drying on water ingress can also be seen from the initial wetting period. During the initial 10-min absorption, for example, it is evident from Fig. 7 that the centre region increases in size at a faster rate than the remainder of the test period which reflects the influence of capillary suction forces resulting from the extended period of drying. The enlargement is more prominent along the directions indicated by arrows due to the presence of the damage to the internal wall of the core region, indicating the preferential movement of water into the inner damaged surface region.

With reference to Fig. 7, it is apparent that the progressive enlargement of the core region is also accompanied by a gradual increase in resistance along the sample boundary, as evidenced by the slight yellow tint which then

gradually turns to darker yellow. This increase in resistance may be a measurement artefact (ringing effect), provided that the normalized resistance displayed an overall decrease in values, although as discussed in section 4.2.1 above, the yellow tint ring may correspond to the slight increase in resistance resulting from the air being pushed into the pore system during the initial few hours of wetting (see Fig. 6(b)). Other supporting evidence from the measurement artefact can be obtained from Fig. 5(b) highlighting that the 'ringing' effect becomes more pronounced as the pipe diameter increases.

Finally, it is interesting to note from Fig. 7 that the increase in resistance between electrodes 2 and 6 appears to cease after approximately 8-hrs absorption. This would, once again, reflect the preferential movement of water into the inner damaged surface region, causing an increase in the degree of pore saturation and thereby decreasing the bulk resistance of the concrete (see the reconstructed images at the remainder of the test period). At 12-hrs, it is evident that the concrete between electrodes 2 and 5 was, indeed, less resistive than the remaining part of the concrete, as indicated by the white and light blue contours. At 20-hrs, it is apparent that this region has increased in size, extending further in the counter-clockwise direction to electrode 16 and in the clockwise direction to electrode 7, which all in agreement with the relatively lower resistance values obtained from direct 4-pt measurements (see Fig. 6). It is observed that another less-resistive region begins to form between electrodes 11 and 12 toward the end of the test period.

5. Concluding remarks

A semi-automated ERT system has been developed that allows automatic current injection and resulting potential measurements at specific time intervals, with image reconstruction being manually performed using the open-source EIT software EIDORS. As an initial study, the system was used to monitor the ingress of water in a hollow cylindrical specimen experiencing surface damage. The reconstructed images obtained from the system were compared with data obtained from direct 4-pt measurements, in order to provide supporting information. The following general conclusions can be drawn from the work presented:

1. It has been shown that the system was capable of providing a reasonable visual representation of non-conductive objects of different diameters placed at varying locations within a cylindrical cell, with tap water being used as the background medium.
2. The system developed is shown to be able to provide the spatial distribution of moisture within concrete. The results indicate that the wetting-front moves more rapidly into the concrete during the

initial period of wetting, with the rate of ingress varying according to the quality of the exposed surface.

3. The results indicate that there was a preferential movement of water into the damaged inner surface region, thereby causing a moisture gradient to develop in the concrete.

Acknowledgements

The authors wish to acknowledge financial support from the School of Energy, Geoscience, Infrastructure and Environment at Heriot-Watt University. Two of the Authors (DS and HMT) also wish to acknowledge the financial support provided by Heriot-Watt University.

References

[1] McCarter, W.J., Ezirim, H., Emerson, M.: Properties of concrete in the cover zone: water penetration, sorptivity and ionic ingress. Mag. Concr. Res. **48(176)**, 149–156 (1996)

[2] McCarter, W.J., Chrisp, T.M., Butler, A., Basheer, P.A.M.: Near–surface sensors for condition monitoring of cover-zone concrete. Constr. Build. Mater. **15(2-3)**, 115–124 (2001)

[3] Thomas, M.D., Bamforth, P.B.: Modelling chloride diffusion in concrete: effect of fly ash and slag. Cem. Concr. Res. **29(4)**, 487–495 (1999)

[4] Ishida, T., Iqbal, P.O., Anh, H.T.: Modeling of chloride diffusivity coupled with non-linear binding capacity in sound and cracked concrete. Cem. Concr. Res. **39(10)**, 913–923 (2009)

[5] Kim, J., McCarter, W.J., Suryanto, B., Nanukuttan, S.V., Basheer, P.A.M, Chrisp, T.M.: Chloride ingress into marine exposed concrete: a comparison of empirical-and physically-based models. Cem. Concr. Compos. **72**, 133–145 (2016)

[6] Weiss, W.J., Yang, W., Shah, S.P.: Shrinkage cracking of restrained concrete slabs. ASCE J. Eng. Mech. **124(7)**, 765–774 (1998)

[7] Mihashi, H., de B Leite, J.P.: State-of-the-art report on control of cracking in early age concrete. J. Adv. Concr. Technol. **2(2)**, 141–154 (2004)

[8] Beaudoin, J.J., MacInnis, C.: The mechanism of frost damage in hardened cement paste. Cem. Concr. Res. **4(2)**, 139–147 (1974)

[9] Bleszynski, R., Hooton, R.D., Thomas,M.D., Rogers, C.A.: Durability of ternary blend concrete with silica fume and blast-furnace slag: laboratory and outdoor exposure site studies. ACI Mater. J. **99(5)**, 499–508 (2002)

[10] Takahashi, Y., Ogawa, S., Tanaka, Y., Maekawa, K.: Scale-dependent ASR expansion of concrete and its prediction coupled with silica gel generation and migration. J. Adv. Concr. Technol. **14(8)**, 444–463 (2016)

[11] Fujiyama, C., Tang, X.J., Maekawa, K., An, X.H.: Pseudo-cracking approach to fatigue life assessment of RC bridge decks in service. J. Adv. Concr. Technol. **11(1)**, 7–21 (2013)

[12] Suryanto, B., Nagai, K., Maekawa, K.: Bidirectional multiple cracking tests on high-performance fiber-reinforced cementitious composite plates. ACI Mater. J. **107(5)**, 450–460 (2010)

[13] Beushausen, H., Alexander, M.G., Andrade, C., Basheer, M., Baroghel-Bouny, V., Corbett, D., d'Andréa, R., Gonçalves, A. , Gulikers, J., Jacobs, F., Monteiro, A.V., Nanukuttan, S.V., Otieno, M., Polder, R., Torrent, R.: Application Examples of Performance-Based Specification and Quality Control. In: Beushausen, H., Luco, L.F. (eds.) Performance-based Specifications and Control of Concrete Durability: State-of-the-Art Report RILEM TC 230-PSC, pp. 197–266. Springer, Dordrecht Heidelberg New York London (2016)

[14] Karhunen, K., Seppänen, A., Lehikoinen, A., Monteiro, P.J.M., Kaipio, J.P.: Electrical resistance tomography imaging of concrete. Cem. Concr. Res. **40**, 137–145 (2010)

[15] Zhang, T., Zhou, L., Ammari, H., Seo, J.K.: Electrical impedance spectroscopy-based defect sensing technique in estimating cracks. Sens. **15(5)**, 10909–10922 (2015)

[16] Hallaji, M., Seppänen, A., Pour-Ghaz, M. Electrical resistance tomography to monitor unsaturated moisture flow in cementitious materials. Cem. Concr. Res. **69**; 10–18 (2015)

[17] Smyl, D. Rashetnia, R., Seppänen, A., M Pour-Ghaz, M.: Can electrical resistance tomography be used for imaging unsaturated moisture flow in cement-based materials with discrete cracks? Cem. Concr. Res. **91**, 61–72 (2017)

[18] Hou, T.C., Lynch, J.P.: Electrical impedance tomographic methods for sensing strain fields and crack damage in cementitious structures. J. Intell. Mater. Syst. Struct. **20(11)**, 1363–1379 (2009)

[19] Hallaji, M., Pour-Ghaz, M.: A new sensing skin for qualitative damage detection in concrete elements: rapid difference imaging with electrical resistance tomography. NDT&E Int. **68**, 13–21 (2014)

[20] Hallaji, M., Seppänen, A., Pour-Ghaz, M.: Electrical impedance tomography-based sensing skin for quantitative imaging of damage in concrete. Smart Mater. Struct. **23**, 085001(2014)

[21] Asgharzadeh, A., Reichling, K., Raupach, M.: Electrical impedance tomography on concrete. Inter. Symp. Non-Destruct. Test. Civ. Eng. (NDT-CE), Berlin, Germany; **19** (2015)

[22] McCarter, W.J., Emerson, M., Ezirim, H.: Properties of concrete in the cover zone: developments in monitoring techniques. Mag. Concr. Res. **47(172)**, 243–251(1995)

411 [23] McCarter, W.J., Chrisp, T.M., Starrs, G., Adamson, A., Owens, E., Basheer, P.A.M., Nanukuttan, S.V.,
412 Srinivasan, S., Holmes, N.: Developments in performance monitoring of concrete exposed to extreme
413 environments. ASCE J. Infrastruct. Syst. **18**, 167–175 (2012)
414 [24] McCarter, W.J., Chrisp, T.M., Starrs, G., Adamson, A., Basheer, P.A.M., Nanukuttan, S.V., Srinivasan, S.,
415 Green, C.: Characterization of physio-chemical processes and hydration kinetics in concretes containing
416 supplementary cementitious materials using electrical property measurements. Cem. Concr. Res. **50**, 26–33
417 (2013)
418 [25] Polydorides, N., Lionheart, W.R.: A Matlab toolkit for three-dimensional electrical impedance tomography:
419 a contribution to the Electrical Impedance and Diffuse Optical Reconstruction Software project. Meas. Sci.
420 Tech. **13(12)**, 1871–1883(2002)
421 [26] Cheng, K.S., Isaacson, D., Newell, J.C., Gisser, D.G.: Electrode models for electric current computed
422 tomography. IEEE Trans. Biomed. Eng. **36(9)**, 918–924 (1989)
423 [27] Adler, A., Guardo, R.: Electrical impedance tomography: regularized imaging and contrast detection. IEEE
424 Trans. Med. Imaging **15(2)**, 170–179 (1996)
425 [28] Brown, B.H., Seagar, A.D.: The Sheffield data collection system. Clin. Phys. Physiol. Meas. **8(A)**, 91–97
426 (1987)
427 [29] BS EN 197-1:2011: Cement: Composition, Specifications and Conformity Criteria for Common Cements.
428 British Standards Institution, London (2000)
429 [30] EIDORS: Electrical Impedance Tomography and Diffuse Optical Tomography Reconstruction Software.
430 http://eidors3d.sourceforge.net/. Accessed 10 July 2016
431 [31] Adler, A., Lionheart, W.R.B.: Uses and abuses of EIDORS: an extensible software base for EIT. Physiol.
432 Meas. **27(5)**, S25–S42 (2006)
433 [32] Adler, A., Arnold, J.H., Bayford, R., Borsic, A., Brown, B., Dixon, P., Faes, T.J., Frerichs, I., Gagnon, H.,
434 Gärber, Y., Grychtol, B.: GREIT: a unified approach to 2D linear EIT reconstruction of lung images. Physiol.
435 Meas. **30(6)**, S35–S55 (2009)
436 [33] Kauppinen, P., Hyttinen, J., Malmivuo, J.: Sensitivity distribution visualizations of impedance tomography
437 measurement strategies. Int. J. Bioelectromagn. **8(1)**, 1–9 (2006)
438 [34] Adler, A., Gaggero, P.O., Maimaitijiang, Y.: Adjacent stimulation and measurement patterns considered
439 harmful. Physiol. Meas. **32(7)**, 731–744 (2011)

[35] McCarter, W.J., Chrisp, T.M., Starrs, G., Holmes, N., Basheer, L., Basheer, P.A.M., Nanukuttan, S.V.: Developments in monitoring techniques for durability assessment of cover-zone concrete. *2nd Inter. Conf. Durab. Concr. Struct.*, Sapporo, Japan (2010)

[36] McCarter, W.J., Chrisp, T.M., Starrs, G., Basheer, P.A.M., Blewett, J.: Field monitoring of electrical conductivity of cover-zone concrete. Cem. Concr. Compos. **27(7)**, 809–817 (2005)

Captions for Tables

Table 1 Concrete mix used in experimental program

Table 2 Oxide analysis of cement

497 **Table 1** Concrete mix used in experimental program

w/c	CEM I kg/m^3	Coarse kg/m^3	Fine kg/m^3	F_{28} MPa
0.7	244	1184	789	21.3

498

499 Note: F_{28} is the 28-day compressive strength measured from 100mm cubes

500

501 **Table 2**: Oxide analysis of cement

By weight %	CEM I
SiO_2	19.67
AI_2O_3	4.84
Fe_2O_3	3.17
CaO	62.58
MgO	2.22
K_2O	0.55
Na_2O	0.17

502

503

504

505

506

507

508

509

510

511

512

513

Captions for Figures

Fig. 1 Schematic diagram of the measurement system.

Fig. 2 Hardware for the EIT measurements and test specimen.

Fig. 3 Test cell (a) without and (b) with the centre pipe; and (c) close-up on the inner circumferential surface of the test specimen after demoulding. Rough and uneven surface texture was evident primarily between 2nd and 5th electrodes.

Fig. 4 Resistivity variation along the outer circumferential surface after 3-month drying in the laboratory environment (20±2^{o}C, 55±5% RH).

Fig. 5 Reconstructed images of difference sizes of PVC pipe placed at different positions in the test cell: (a) a 48-mm PVC pipe positioned in front of electrode 1 and 9; (b) a 48-mm, 64-mm and 88-mm pipe positioned at the centre of the cell. The actual position of the PVC pipe is denoted with a dashed line. The colour bar is provided, with dark red representing a significant relative increase in resistance, white representing no relative change, and dark blue representing a significant relative decrease in resistance.

Fig. 6 Normalized resistance during the initial 20-hours, with measurements taken from two adjacent pairs of electrodes along the outer circumferential surface: (a) data obtained from the right-half side of the specimen (between pins 1 and 9, in clockwise direction); and (b) data from the other half of the specimen.

Fig. 7 Reconstructed images during absorption. These images show the preferential movement of water into the damaged inner surface region.

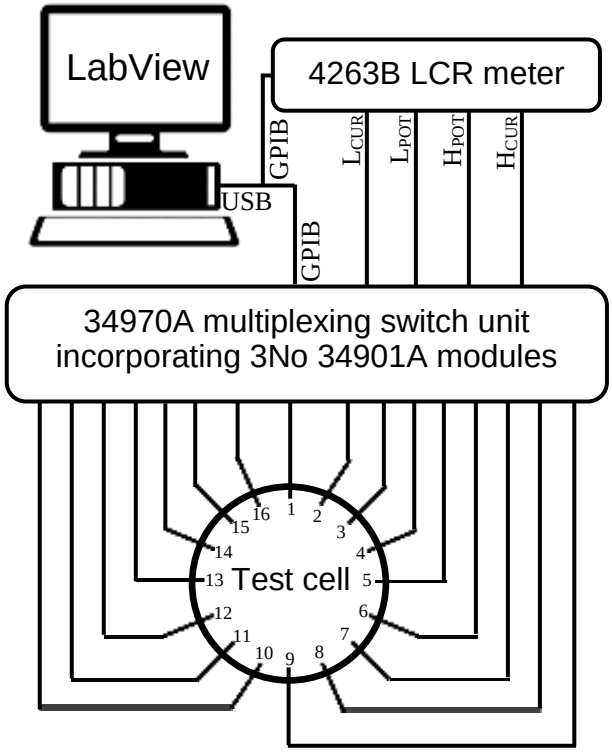

Fig. 1 Schematic diagram of the measurement system.

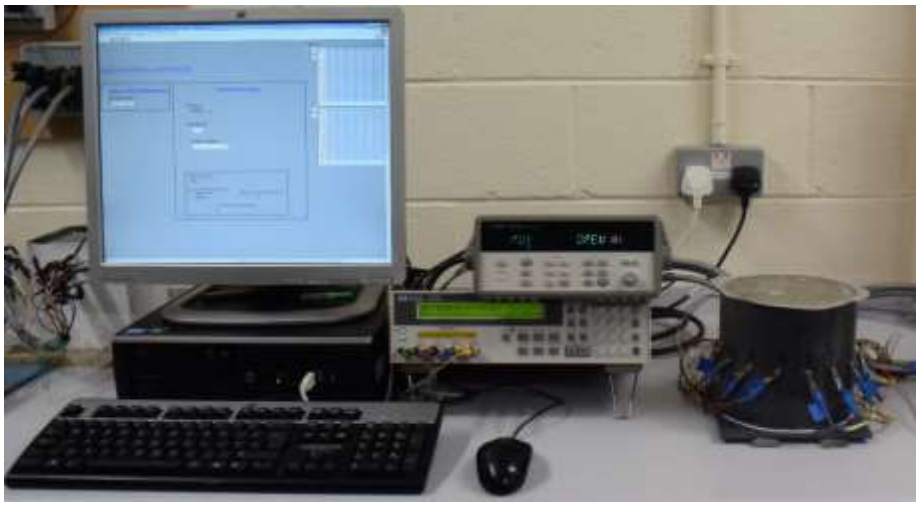

Fig. 2 Hardware for the EIT measurements and test specimen.

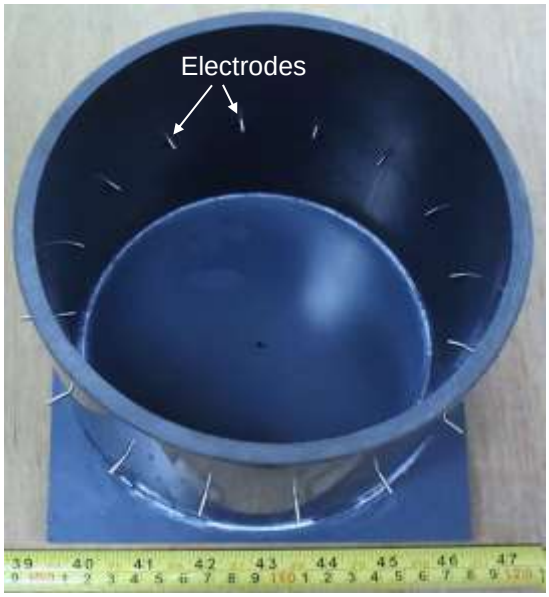

(a)

(b)

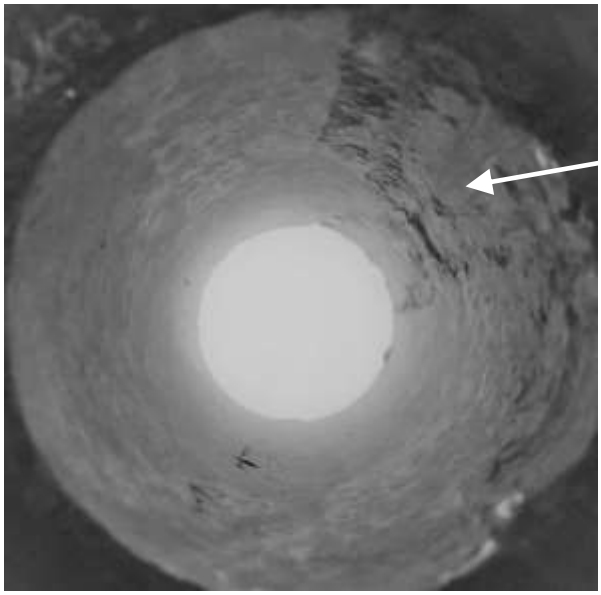

(c)

Fig. 3 Test cell (a) without and (b) with the centre pipe; and (c) close-up on the inner circumferential surface of the test specimen after demoulding. Rough and uneven surface texture was evident primarily between 2nd and 5th electrodes.

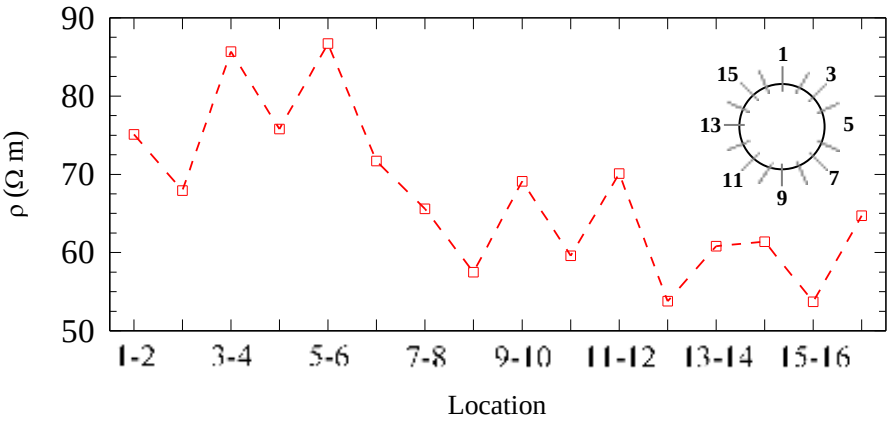

Fig. 4 Resistivity variation along the outer circumferential surface after 3-month drying in the laboratory environment (20±2ºC, 55±5% RH).

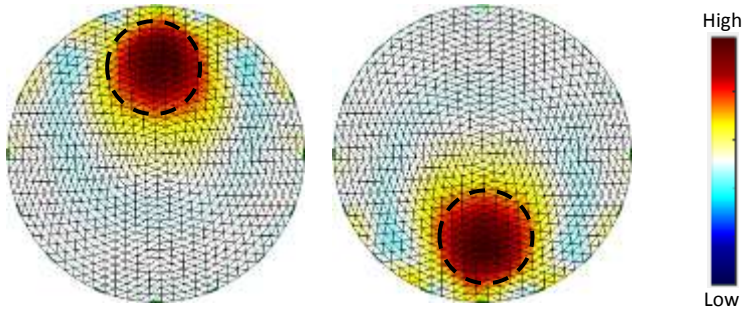

(a)

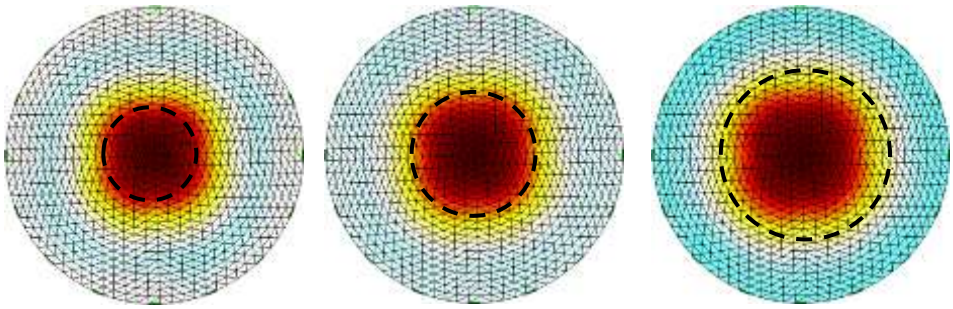

(b)

Fig. 5 Reconstructed images of difference sizes of PVC pipe placed at different positions in the test cell: (a) a 48-mm PVC pipe positioned in front of electrode 1 and 9; (b) a 48-mm, 64-mm and 88-mm pipe positioned at the centre of the cell. The actual position of the PVC pipe is denoted with a dashed line. The colour bar is provided, with dark red representing a significant relative increase in resistance, white representing no relative change, and dark blue representing a significant relative decrease in resistance.

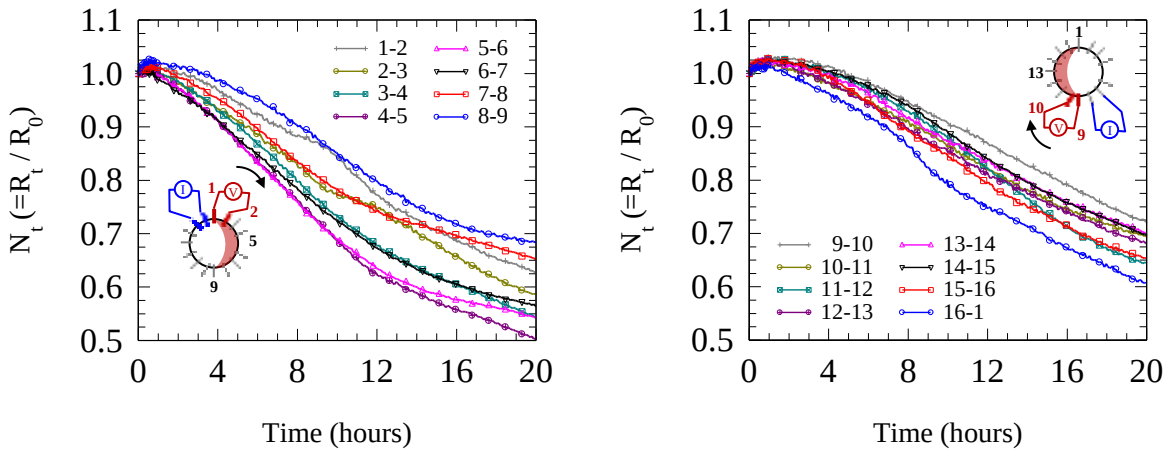

Fig. 6 Normalized resistance during the initial 20-hours, with measurements taken from two adjacent pairs of electrodes along the outer circumferential surface: (a) data obtained from the right-half side of the specimen (between pins 1 and 9, in clockwise direction); and (b) data from the other half of the specimen.

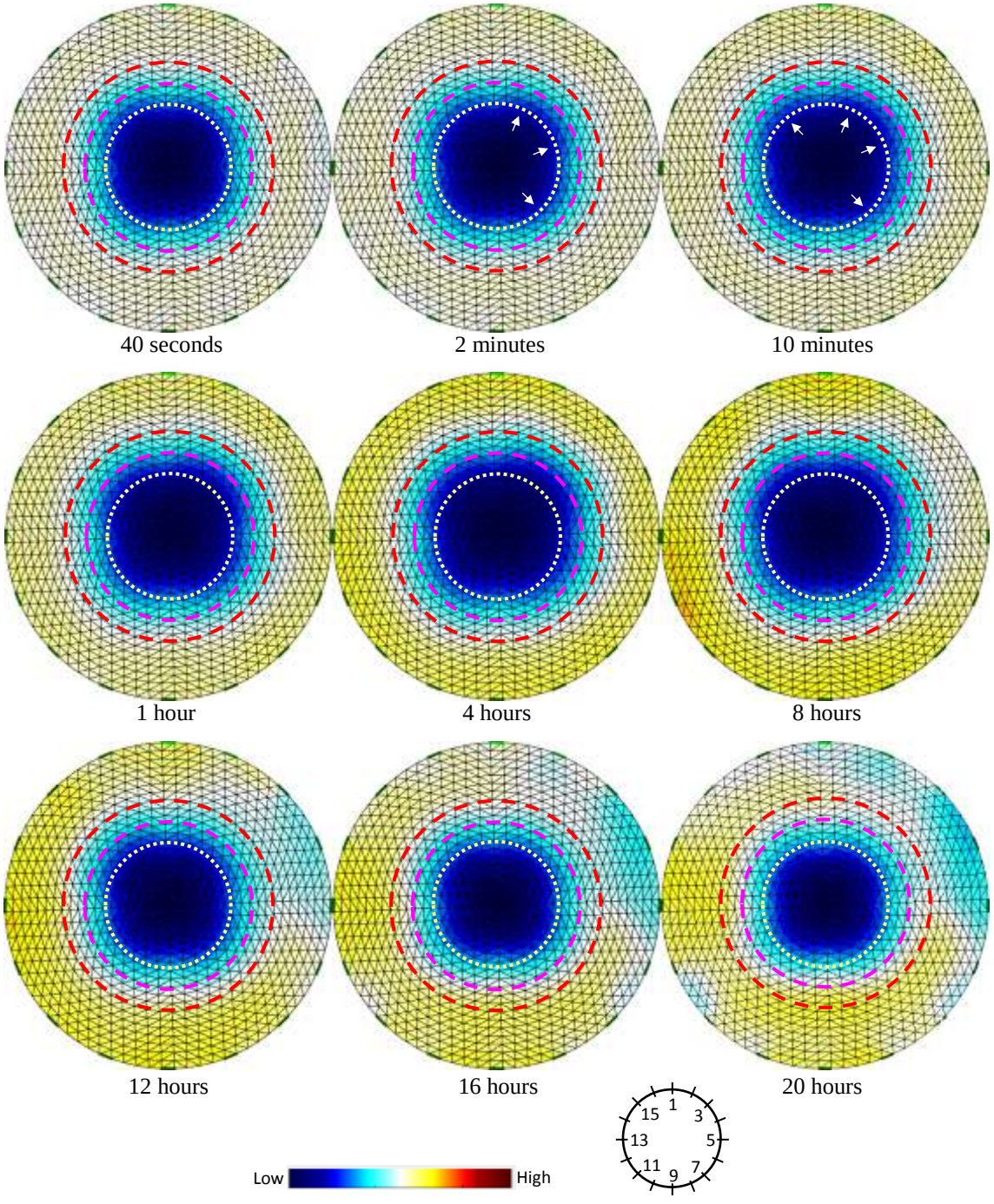

Fig. 7 Reconstructed images during absorption. These images show the preferential movement of water into the damaged inner surface region.